Finite element modelling of hydraulic fracturing on a reservoir scale in 2D

Magnus Wangen[a]

[a]*Institute for Energy Technology P.O.Box 40, N-2027 Kjeller, Norway*

Abstract

A finite element based procedure is suggested for the modelling of hydraulic fracturing of heterogeneous rocks on a macroscopic scale. The scheme is based on the Biot-equations for the rock, and a finite element representation for the fracture pressure, where the fracture volume appears as fracture porosity. The fracture and the rock are represented unified on the same regular finite element grid. The numerical solutions of pressure and displacement are verified against exact 1D results. The 1D model also shows how the tension forces that open the fracture decreases as the gradient of the pore pressure decreases. The fracture criterion is based on the "strength" of bonds in the finite element grid. It is shown how this criterion scales with the grid size. It is assumed that fracturing happens instantaneously and that the fluid volume in the fracture is the same after a fracture event. The pressure drop that follows a fracture event is computed with a procedure that preserves the fluid volume in the fracture. The hydraulic fracturing procedure is demonstrated on a homogeneous and an inhomogeneous rock when fluid is injected at a constant rate by a well at the centre of the grid. A case of a homogeneous rock shows that a symmetric fracture develops around the well, where one bond breaks in each fracture event. A heterogeneous case shows the intermittent nature of the fracture process, where several bonds break in each fracture event.

Keywords: hydraulic fracturing, pressure-transients, intermittent process, fracture criteria, fracture propagation, heterogeneity, finite element method (FEM), 2D

Email address: `Magnus.Wangen@ife.no` (Magnus Wangen)

1. Introduction

Hydraulic fracturing of rock is the process where the pore pressure build-up, for instance by an injection well, becomes sufficiently high to fracture the rock (Jaeger et al., 2007). It is commonly applied by the oil industry to enhance the permeability of the near well region of reservoirs. Hydraulic fracturing has become necessary in production of shalegas, where one wants to fracture a maximum of shale at a minimum of expenses (Cheng et al., 2007). Similar considerations apply for deep geothermal wells (Evans et al., 2005; Sanjuan et al., 2006) where "good" communication between injection and production wells is important for energy production. Another related field is safe and secure storage of CO_2 in aquifers and reservoirs, where enhanced injectivity in the near-well region can be achieved by hydraulic fracturing. At the same time, it is important that CO_2 injection can be carried out with a minimum risk for fracturing of the reservoir seal, which may cause leakage of CO_2 (Rutqvist and Tsang, 2002; Kvamme and Liu, 2009).

Hydraulic fracturing also occurs naturally as a fluid release mechanism during pressure build-up in reservoirs over geological time (Sibson, 1992; Wangen, 2001). Other examples are melt segregation and eruption in the crust (Jackson et al., 2003), melt intrusion as sills and dykes (Turcotte and Morgan, 1992), mud volcanos and hydrothermal megaplumes (Judd and Hovland, 2007).

Much of the current knowledge of hydraulic fracturing at a reservoir scale comes from the oil industry where it has been a technique to enhance the flow properties of rocks with low permeability. The propagation of hydraulic fractures can be observed with passive seismic monitoring, and the seismic events can be correlated with the well head pressure and the injection rate (Weng et al., 1997; Sasaki, 1998; Rector et al., 2000). The interpretation of the seismic events may be complicated by activation of slip along faults as the pore pressure increases and the effective stress decreases (Sasaki, 1998). Seismic observations show that hydraulic fracturing is an intermittent process, but the actual texture of the fractures is very difficult to observe at a reservoir scale. The complex nature of fluid flow in fractures adds to the complexity, because fractures have a rough surface and the flow inside them are non-evenly distributed (Bernabé, 1995; Brown et al., 1998; Alava et al., 2006).

Although the importance of hydraulic fracturing, both in reservoir engineering and as a natural process, it is still a very challenging process to model. Modelling

fracture nucleation, propagation and interaction is challenging even without the pore fluid as the cause for fracturing. The fractures are discontinuities in the solid, and they are normally complex structures, due to the heterogeneous nature of rocks. Such complex discontinuities are not easily represented by standard finite difference or finite element grids (Alava et al., 2006).

Different types of models have been developed for hydraulic fracturing. The first models applied by the oil industry were based on known (analytical) results for fractures (Hubbert and Willis, 1957). These models have loading of the fracture walls by an internal fluid pressure and they were added leak-off through the fracture walls. Such semi-analytical models for hydraulic fracture were later integrated with numerical reservoir simulators (Settari, 1979). A development that has continued until today, see Adachi et al. (2007) for a review. A particular shortcoming of these models is that they do not easily handle the heterogeneities that exist in rocks on all length scales. How heterogeneities control fracture nucleation, propagation and interaction have been studied with simple models like the random fuse model and models made of springs and beams, see Herrmann and Roux (1990) for a review. These models of deformation and fracture have later evolved into models of hydraulic fracture like the beam model (Tzschichholz et al., 1994; Tzschichholz and Herrmann, 1995; Tzschichholz and Wangen, 1998) and the spring model (Flekkøy et al., 2002). Distinct element code has been developed to study fracturing and later extended with pore fluid to study hydraulic fracturing (Al-Busaidi et al., 2005). Finally, finite element models are developed, which build on Biot's equations for poroelasticity, where the fractures are handled by changes in the permeability field (see for example Tang et al. (1992); Wang et al. (2009)).

This study deals with macroscopic hydraulic fracture of heterogeneous rock at a reservoir scale. The modeling is 2D and the spatial discretization is done with the finite element method using square bilinear elements. The grid has an element size that is typically $1\text{m} \times 1\text{m}$ both for the rock and the fracture. However, the elements that represent the rock are treated differently from those of the fracture. The rock is assumed to follow the Biot equations for poro-elasticity. The elements that contain the fracture are modelled with a pressure equation where the fracture volume is accounted for by the fracture porosity. The representation of both the rock and the fracture by the same regular grid simplifies the numerical formulation. It also makes fluid pressure in the fracture fully integrated with the fluid flow in the rock. An essential feature of the macroscopic model is that it represents

the pressure gradients that open the fracture. It is then possible to model macroscopic stress distribution around the fracture and fracture propagation. Although a coarse grid resolution is unable to capture the complex details of fractures at a micro-scale.

We apply a fracture criterion that utilizes the strain measured by bonds defined by the element sides. The fracture criterion is analogous to the beam strength of beam models (Tzschichholz et al., 1994; Tzschichholz and Herrmann, 1995; Tzschichholz and Wangen, 1998), spring strength of spring models (Flekkøy et al., 2002), and it makes it easy to include randomness which allows for the modeling of heterogeneous rocks. A simple procedure is suggested and demonstrated for the calculation of the pressure drop that follows a fracture event.

The paper is organized as follows: The Biot equations are first introduced. Then follows a presentation of the fracture criterion, the time stepping, the discretization of the fracture, the fluid pressure in the fracture and the permeability of fractured elements. The verification of the code is presented by means of 1D solutions and fracture aperture. The grid size dependence of the fracture criterion is discussed before examples are shown. One case is a homogeneous rock and the other is a heterogeneous rock.

2. The Biot equations for the rock

The fracture model is based on Biot's equations for coupled deformations and fluid flow in porous media (Biot, 1941; Wang, 2000). The equilibrium equations are

$$\frac{\partial \sigma_{ij}}{\partial x_j} = -\varrho_b \delta_{i3} \tag{1}$$

where σ_{ij} is the stress tensor and ϱ_b is the bulk density of the rock. The indices i and j run over the spatial directions $x = 1$ and $y = 2$ in a 2D horizontal reservoir. The right-hand-side is therefore zero since gravity acts in the vertical direction ($z = 3$). Effective stress is related to strain by the Lamé-equations

$$\sigma'_{ij} = \sigma_{ij} - \alpha p \delta_{ij} = -\Big(\lambda \epsilon_{kk} \delta_{ij} + 2G\epsilon_{ij}\Big) \tag{2}$$

where p is the fluid pressure and ϵ_{ij} is the strain

$$\epsilon_{ij} = \frac{1}{2}\Big(\frac{\partial u_i}{\partial x_j} + \frac{\partial u_j}{\partial x_i}\Big) \tag{3}$$

and where u_i is the displacement in the i-direction. (Einstein summation convention is applied which assumes summation over each pair of equal indices.) The minus sign is introduced in the stress-strain relation (2) in order to have compression corresponding to positive effective stress and tension to negative effective stress. The Lamé parameters λ and G are given by the Young's modulus E and the Poisson ratio ν as

$$\lambda = \frac{\nu E}{(1+\nu)(1-2\nu)} \quad \text{and} \quad G = \frac{E}{2(1+\nu)} \tag{4}$$

The equilibrium equations (1), the Lamé-equations (2) and the expression (3) for strain make together the equations for the displacement field

$$\Big(\lambda + G\Big)\frac{\partial^2 u_k}{\partial x_k \partial x_i} + G\frac{\partial^2 u_i}{\partial x_k \partial x_k} - \alpha\frac{\partial p}{\partial x_i} = 0 \tag{5}$$

Boundary conditions for this equation are zero displacement normal to the boundaries. The corresponding pressure equation is

$$S\frac{\partial p}{\partial t} - \nabla\Big(\frac{k}{\mu}\nabla p\Big) = -\alpha\frac{\partial \epsilon}{\partial t} \tag{6}$$

where S is the specific storage coefficient, $\epsilon = \epsilon_{11} + \epsilon_{22} + \epsilon_{33}$ is the volume strain, k is the permeability and μ the viscosity. The pressure equation is solved with zero pressure at boundaries. The initial pressure is taken to be zero and the initial displacements are also zero.

We notice from the Lamé equations (5) that non-zero displacements are the result of pressure gradients. From the pressure equation (6) we see that changes in the volume-strain act as a source term. In the applications we will study hydraulic fracturing from fluid injection at the centre of the grid. Fluid flow from injection then dominates over changing volume strain through time. It is then, for such cases, possible to solve the equations for pressure and displacement decoupled, since the displacement field (volume strain) has negligible effect on the pressure. The pressure equation (6) is solved first, and then the displacement field with the given pressure solution. The time-dependency in the displacement equation is from the time-dependency of the pressure, and it is therefore the pressure field that controls the displacement field.

The appendix gives a summary of the finite element formation of Lamé equation (5) and the pressure equation (6).

3. Fracture criterion

The criterion that decides when the rock fails is an essential part of any code for fracture modelling. We have chosen a criterion based on the strength of the bonds defined by the element sides. These bonds become stretched in elements under tensile stress. The criterion is therefore restricted to tensile (mode I) fractures. The bonds are assigned a fracture threshold, which is the maximum strain before breaking.

The fracture is produced by injecting fluid at the centre of the grid and letting the fluid pressure increase. Once the fluid pressure has increased sufficiently for a bond to become stretched beyond its threshold it breaks. The centre element (or the well) and the two opposite neighbour elements are the initial cavity that propagates as a fracture. The fracture surface becomes inspected for over-stretched bonds at the end of each time step.

The element that has a broken bond as a side becomes a part of the fracture, which means that this element changes properties from rock to fracture. A fracture element becomes different from a rock element by having a reduced Young's modulus and an increased permeability. A very low value for Young's modulus is used as an alternative to removing the fractured elements from the finite element computation for the displacements.

We will look at hydraulic fracture of both homogeneous and inhomogeneous rock. An homogeneous rock has bonds with the same strength threshold, while an inhomogeneous rock has a random distribution of bond strengths. The random bond strength may be either quenched or annealed. Quenched disorder means that the disorder is "frozen" in the grid. Annealed disorder is when the randomness is allowed to change with time. Our model has quenched disorder. The bond strength is initialized at the beginning of a computation using the following distribution

$$s = \bar{s}\frac{(r+2)}{(r+1)}\psi^{1/(r+1)} \tag{7}$$

taken from (Tzschichholz et al., 1994; Tzschichholz and Herrmann, 1995). The random variable ψ is uniformly distributed between 0 and 1, $\bar{s}$ is the average bond strength and the parameter r controls the width of the distribution. The distribution becomes narrow for large r, because $s \to \bar{s}$ when $r \to \infty$. A wide distribution is obtained with r close to -1, in which case some bonds get a strength in the neighborhood of $\bar{s}$ and other bonds become very weak. A homogeneous

rock is simply made by assigning the same strength $\bar{s}$ to all bonds, and the example of a strongly heterogeneous rock (presented later) has $r = -0.3$.

4. Time stepping

The time step is set to a minimum value when a fracture event happens in order to compute the following transients in the fluid pressure. The time step is increased by a constant factor if there are no fracture events. It is then possible to do time stepping through long periods with only pressure build-up. The factor is normally in the range from 1.2 to 2, which allows the time step to be increased by a factor 1000 after ~ 40 to ~ 10 steps, respectively. The minimum time step is 1 s in the examples. There is also a maximum time step, and there is no increase in the time step once the maximum step is reached.

5. Discretization of the fracture

We want to model the fracture using the same regular FEM-grid as the surrounding rock. Mass conservation of fluid in the fracture is the starting point for making such a FEM-formulation. Mass conservation requires that the rate of injection at the well is equal to the rate of mass accumulation in the fracture plus the rate of mass leakage though the fracture walls. This is written as

$$\frac{d}{dt}\int_V \varrho_f \, dV + \int_{\partial V} \varrho_f \mathbf{v}_D \cdot \mathbf{n} \, dA = \dot{M}_{\text{in}} \tag{8}$$

where V is the volume of the fracture and ∂V is the fracture surface. The first term in equation (8) is the rate of mass accumulation in the fracture and the second is the rate of leakage through its surface. The Darcy flux $\mathbf{v}_D$ is in the rock right outside the fracture and $\mathbf{n}$ is the outward unit normal of the fracture surface. The right-hand-side is the rate of mass injection $\dot{M}_{\text{in}} = \varrho_f Q_{\text{in}}$, where Q_{in} is the volume rate of injection.

Equation (8) for mass conservation of fluid in the fracture can be approximated by the elements in the grid. Figure 1 shows a linear fracture and the elements that are traversed by it. The volume of these elements is V_E. The surface integral is approximated by sum over the Darcy fluxes around the fractured elements. The leakage from the fracture is dominated by flow normal to the sides, which in

the FEM-grid are given by the fluxes in the neighbour elements to the fracture. The mass of fluid in the fracture can be represented by a volume integral over the fractured elements by introducing fracture porosity ϕ_c, which is the volume fraction of fracture in the element. The rate of mass accumulation in the fracture can then be written as

$$\frac{d}{dt}\int_V \varrho_f dV = \frac{d}{dt}\int_{V_E} \phi_c\, \varrho_f dV_E \tag{9}$$

and the finite element expression for mass conservation in the fracture becomes

$$\frac{d}{dt}\int_{V_E} \phi_c \varrho_f\, dV + \int_{\partial V_E} \varrho_f \mathbf{v}_D \cdot \mathbf{n}\, dA = \dot{M}_{\text{in}} \tag{10}$$

The time-derivation goes through the integration sign because the volume V_E is constant. Gauss theorem converts the surface integral to a volume integral which gives the following pressure equation for the fractured elements

$$\phi_c c_f \frac{\partial p}{\partial t} - \nabla\Big(\frac{k_c}{\mu}\nabla p\Big) = \begin{cases} -\partial\phi_c/\partial t & \text{(outside injection element)} \\ Q_{\text{in}}/h^2 & \text{(for injection element)} \end{cases} \tag{11}$$

where Q_{in}/h^2 is the injection rate per element volume. It is now assumed that fluid flow in fracture is by Darcy's law given by a fracture permeability k_c. The fracture permeability is discussed section 7. An essential property of the fracture permeability is that it sufficiently large to prevent large pressure drops inside the fracture zone.

The computation of the fracture porosity is straightforward for each element in the fracture zone. It is simply the volume fraction of void from the fracture

$$\phi_c = \frac{A - A_0}{A_0} \tag{12}$$

where A_0 and A are the areas of an undeformed and a deformed element, respectively. The coordinates of the deformed element are obtained by adding the deformations. The displacements of the nodes of the fractured elements therefore give the fracture width.

The time-derivative of the fracture porosity is obtained by numerical derivation and it is computed from the two last time steps. This works fine in the numerical scheme because it does not change much from time step to time step during pressure build-up.

The pressure equations (6) and (11), for the rock elements and the fracture elements, respectively, are of the same form and covers the regular finite element grid. The numerical formulation for the pressure in the fracture is therefore unified with the fluid flow in the rock.

Equation (8) for mass conservation in the fracture shows two regimes with respect to the injection rate. The first regime is case of an impermeable (or low permeable) rock where the leakage through the fracture walls are much less than the injection rate. The time-rate of increasing fracture volume can then be approximated as

$$\frac{dV}{dt} \approx Q_{\text{in}} \tag{13}$$

assuming that the pore fluid is incompressible. The other regime is when all the injected fluid leaks through the fracture walls

$$\int_{\partial V} \mathbf{v}_D \cdot \mathbf{n}\, dA = Q_{\text{in}} \tag{14}$$

This case represents the stationary state where the fracture volume is constant.

6. Fluid pressure in the fracture

The breaking of a bond leads to a pressure drop in the fracture. It is because the fracture becomes longer, while the fluid volume in the fracture does not change. The aperture therefore decreases, and less pressure is required to maintain a reduced fracture opening. We assume that the fluid pressure inside the fracture is nearly the same everywhere, and that the pressure drop happens instantaneously. The pressure drop will therefore only affect the nodes of the fracture, (which are along its surface).

The pressure drop is computed with separate procedure. The volume of the fracture is known before a bond is broken. The fracture pressure has to be reduced for the fracture volume to remain the same after a fracture event. This is done with a Newton scheme. A function that computes the fracture volume from knowledge of the fracture pressure is used. A fracture pressure is assigned the fracture nodes, and the corresponding displacements and fracture volume are then computed. The Newton step uses numerically computed derivatives, and convergence is rapid because changes in fracture volume and fracture pressure are nearly linearly related. Only two Newton iterations are needed to obtain a pressure increment that is less than 1 Pa.

7. The permeability of fractured elements

The fractured elements are assigned a constant permeability, which represents the increased average permeability caused by the fracture. It is possible, by comparing the fracture width with a minimum width, to check when the average element permeability is dominated by the fracture. A fractured element becomes more permeable in the direction of the fracture. It is straightforward to estimate this permeability when we assume that it is cut by a parallel plate fracture aligned with the element sides. The average permeability in the direction of the fracture is then

$$k_{\mathrm{av}} = \left(1 - \frac{w}{h}\right)k_r + \left(\frac{w}{h}\right)k_f \quad \text{and} \quad k_f = \frac{1}{12}w^2 \tag{15}$$

where k_r is the rock permeability, k_f is the fracture permeability, h is the element size and w is the fracture aperture. The condition for the fracture to dominate the average permeability is simply

$$w \gg w_{\min} = (12k_r h)^{1/3} \tag{16}$$

when the element size is much larger than the fracture aperture. An element with a size and permeability as large as $h = 10$ m and $k_r = 1 \cdot 10^{-12}$ m^2, respectively, becomes dominated by a fracture with an aperture as low as $w > w_{\min} = 0.5$ mm. The average permeability of elements with smaller size or lower rock permeability becomes dominated by fractures with smaller apertures. The average permeability normal to the fracture becomes negligibly increased.

Flekkøy et al. (2002) applied an anisotropic parallel-plate permeability for the fracture zone in a 2D model. Such an approach models the physics accurately on a short length scale when the fracture zone appears as parallel plates. On the length scale of several meters it appears that tension fractures are complex zones of branches and micro-fractures (Davis and Reynolds, 1996). The fracture surface is not plane either, instead they are rough. It appears that a wide range of brittle material has statistically the same roughness (Måløy et al., 2003, 2006). The roughness leads an uneven flow in the fractures, which is characterized by channels (Brown et al., 1998).

The numerical case studies in 2D have fractures where the permeability, equation (15), is much larger than the permeability of the rock. The permeability of the fracture can in some 2D cases become more than 10 orders of magnitude larger than for the rock, for instance $k_r \approx 10^{-18}$ m^2 and $k_f \approx 10^{-8}$ m^2. A very large difference in permeability between the rock and the fracture may be challenging for

iterative linear equation solvers. A limit on the fracture permeability has therefore been applied to make the numerical solution well behaved. The specific value of the fracture permeability is less important as long as it is large enough for pressure to be nearly constant in the fracture.

8. Verification of the numerical solution

The Lamé equations (5) for the displacement are considerable simplified in 1D. Assuming that displacement u is in the x-direction gives that

$$\frac{\partial^2 u}{\partial x^2} = \frac{1}{(2G+\lambda)}\frac{\partial p}{\partial x} \tag{17}$$

in the time-dependent case. The Biot coefficient is for simplicity taken to be $\alpha = 1$. Integration of equation (17) two times leads to the displacement

$$u(t,x) = \frac{1}{(2G+\lambda)}\left(\int_0^x p(t,x')dx' - p_0 x\right) \tag{18}$$

when boundary conditions are $u = 0$ at $x = 0$ and $du/dx = 0$ at $x = l$. The latter boundary condition follows from zero effective stress ($\sigma'_{xx} = 0$) at the fracture wall at $x = l$. The effective stress is zero because the pressure (p) is equal to the stress (σ_{xx}) in the walls of the fractures. Zero effective stress $\sigma' = -(2G + \lambda)\, du/dx = 0$ gives that $du/dx = 0$. The pressure at the boundary $x = l$ has the constant value p_0.

Pressure rises instantaneously in the fracture from zero to p_0 at time $t = 0$, and the pressure equation has therefore zero pressure as initial condition. The boundary conditions are $p = 0$ at $x = 0$ and $p = p_0$ at $x = l$, respectively. This equation is made dimensionless by introducing the scaled variables, $\hat{p} = p/p_0$, $\hat{x} = x/l$, and $\hat{t} = t/t_0$, where the characteristic time is

$$t_0 = \frac{S\mu l^2}{k} \tag{19}$$

The time t_0 is the time scale needed for the pressure to reach steady state. The pressure equation is then dimensionless

$$\frac{\partial \hat{p}}{\partial \hat{t}} - \frac{\partial^2 \hat{p}}{\partial \hat{x}^2} = 0 \tag{20}$$

assuming that the term $\partial\epsilon/\partial t$ is negligible. The initial condition is $\hat{p} = 0$ and the boundary conditions are $\hat{p} = 0$ for $\hat{x} = 0$ and $\hat{p} = 1$ for $\hat{x} = 1$. The solution of the dimensionless pressure equation is by separation of variables

$$\hat{p}(\hat{t}, \hat{x}) = \hat{x} + \sum_{n=1}^{\infty} a_n \sin(\lambda_n \hat{x}) \exp(-\lambda_n^2 \hat{t}) \tag{21}$$

where

$$a_n = \frac{2\,(-1)^n}{\lambda_n} \quad \text{and} \quad \lambda_n = n\pi \tag{22}$$

The pressure with units follows from the definition of the dimensionless variables and it is

$$p(t, x) = p_0\, \hat{p}(t/t_0, x/l) \tag{23}$$

We notice that the Fourier series decay to zero with time and that the pressure approaches the stationary pressure $p_s = p_0 x/l$. The first term in the series has the slowest decay towards zero and the largest Fourier coefficient. It can therefore be used to estimate the half life of the pressure decay, which becomes

$$\hat{t}_{1/2} \approx \frac{\log 2}{\pi^2} \approx 0.07 \quad \text{or} \quad t_{1/2} \approx 0.07\, t_0 \tag{24}$$

The time scale for the pressure decay is controlled by the characteristic time t_0, and the pressure will be far away from a stationary state for time spans that are less than $t_{1/2}$. This is also important with respect to how fast the pressure build-up approaches the boundary. Pressure build-up from fluid injection and changes in the displacement field will not reach the boundaries for time intervals less than $t_{1/2}$. In the following we will assume that the compressibility of the fluid is more important than the compressibility of the porous matrix. The specific storage can then be approximated as

$$S = \phi c_f \varrho_f \tag{25}$$

where ϕ is the rock porosity, c_f is the fluid compressibility and ϱ_f is the fluid density.

Figure 2 shows the pressure solution (23) after a constant pressure $p_0 = 10$ MPa is applied at the left boundary. The grid size is 100m $\times$ 100m and the resolution is 20×20 nodes. The length of the rock from the fracture to the boundary is $l = 47.4$ m, the permeability is $k = 1 \cdot 10^{-15}$ m^2, the porosity is $\phi = 0.2$, the fluid viscosity is $\mu = 1 \cdot 10^{-3}$ Pa s, the compressibility is $c_f = 1 \cdot 10^{-8}$ Pa^{-1} and the density is $\varrho_f = 1 \cdot 10^3$ kg m^{-3}. The pressure along the profile is plotted first for time

$t = 0.2$ days and then for the time steps 0.6, 1.4, 3, 6.2, 12.6, 25.4 and 50.8 days. We see that there is no pressure build-up close to the boundary for $t < 2$ days, which is consistent with the time scale in this case, which is $t_0 = 231.5$ days and $t_{1/2} = 16$ days. At the nearly steady state ($t = 50.8$ days) the pressure is increasing linearly from the hydrostatic (left) boundary to the fracture wall (right). Figure 2 shows also the nodal-values of the numerical pressure solution, which are in accordance with the exact solution.

Figure 3 shows the displacement field through the rock as the pressure is increasing with time. The absolute value of the displacement at the fracture wall ($x = l$) begins at the maximum value

$$|u|_{\max} = \frac{p_0 l}{(2G + \lambda)} \tag{26}$$

at $t = 0+$, which is immediately after the pressure has been applied. The absolute value then decreases as the pressure moves into the rock, and it becomes reduced to the half

$$|u|_{\min} = \frac{1}{2} |u|_{\max} \tag{27}$$

as the pressure approaches steady state. This is also seen from the expression for the displacement (18), where the integral over the pressure increases from -1 to $p_0 l/2$ as the pressure increases from the initial value $p = 0$ to the stationary value $p(x) = p_0 x/l$. The numerical solution for the node displacements is also shown in Figure 3, and the agreement is good although the numerical solution is coarse (only 10 nodes through the rock). The elastic parameters $E = 50$ GPa and $\nu = 0.25$ ($G = 20$ GPa and $\lambda = 20$ GPa) gives that $|u|_{\max} = 7.89$ mm and $|u|_{\min} = 3.9$ mm for $p_0 = 10$ MPa as seen from Figure 3. Figure 4 shows the displacement at the fracture wall as a function of time, and transient behaviour is the same as for the pressure.

The effective stress through the rock becomes

$$\sigma'(t, x) = -(2G + \lambda)\frac{\partial u}{\partial x} = p_0 - p(t, x) \tag{28}$$

and the stress is therefore $\sigma(t, x) = \sigma' + p(t, x) = p_0$. The energy stored in the 1D rock with a unit cross section $A_0 = 1$ m^2 is

$$W(t) = \frac{1}{2} A_0 \int_0^l \sigma\epsilon \, dx = \frac{p_0}{2(2G + \lambda)} \left(\int_0^l p(t, x')dx' - p_0 l \right) \tag{29}$$

and it is plotted in Figure 5. The transient behaviour of the energy is also dictated by the transient pressure. Using the same numbers as above in the expression for the energy gives that it is initially $W(0+) = 39.5$ kJ, and that the energy decreases to the half as the pressure approaches steady state. Figure 5 shows the numerically computed energy at the same time steps as for the pressure. It is in good agreement with the analytical expression for the energy (29).

The displacement can be expressed in dimensionless form as

$$\hat{u} = \frac{u}{l} = -N \cdot \Big(\int_0^{\hat{x}} \hat{p}(\hat{x}')d\hat{x} - \hat{x} \Big) \tag{30}$$

where

$$N = \frac{p_0}{(2G + \lambda)} \tag{31}$$

is the only explicit parameter in this 1D model for coupled fluid pressure and stress/strain in the porous rock. It should be noted that the 1D results were computed with the 2D code, the same code as in the 2D simulations demonstrated in the next sections.

The 1D solutions for pressure and displacement apply for an infinite long fracture. These solutions are therefore not suited to test the computation of the width (aperture) of a fracture with finite length. The fracture width is given by the node displacements of the fractured elements. Figure 1 shows the nodes at the surface of a linear fracture in the x-direction. The computed displacement in the y-direction of these nodes gives the shape and width (aperture) of the fracture. The numerical solution was tested by computing the width of a predefined linear fracture with a constant fluid pressure. The numerically computed node displacements of the fracture elements are then compared with the analytical solution for displacement

$$u_y(x) = \pm \frac{2(1-\nu^2)p_0}{E}(a^2 - x^2)^{1/2} \tag{32}$$

which applies for a 2D plain-strain fracture in an infinite domain, when it is loaded with a constant fluid pressure p_0 (Sneddon and Elliott, 1946; Helland, 1984). The fracture extends a distance a along the x-axis on both sides of the origin. Solution (32) gives an elliptical fracture shape with a maximum width $w_{\max} = 4(1-\nu^2)\, p_0\, a^2/E$ at the center. A numerical test on a 2D square grid, where the fracture length $2a$ is 20% of the grid size (length of one grid side), gives an elliptic fracture with a width that is 85% of the width from the analytical solution (32). A plot of the y-displacements of the nodes along the fracture surface

as a function of the x-coordinate gives the fracture shape. Figure 1 shows these nodes along the fracture. The fracture width is the difference in displacement at the opposite sides of the fracture, which is the difference in y-displacement of the nodes of the broken bonds shown in figure 1. Recall that the numerical solution has zero displacement normal to the external grid boundaries, and that the analytical solution (32) applies for an infinite domain. The computed fracture aperture approaches the analytical solution (32) as the grid size increases relative to the fracture length.

9. Grid size dependence

The fracture criterion is based on the strain of the bonds (the element sides) which makes the breaking threshold dependent on the grid size. This is observed for the bonds at the two tips of a straight crack. These are the most stretch bonds for a homogeneous rock. In order to investigate the grid size dependence we computed the average strain at the tips of a straight fracture for different grid resolutions. All other conditions were kept constant, like for instance the same stationary fluid pressure. The strain at the crack tip is plotted as a function of resolution in Figure 6, where the resolution is measured by the block size $h = l/N$, and where N is the number of nodes in one spatial direction. The total number of grid nodes in 2D is $N \times N$ nodes. The Figure 6 shows that the strain scales as $\sqrt{N}$ when the system size l is kept constant. We therefore observe that the strain at the tips of a straight crack increases as the grid resolution increases. This observation can be shown by using the $1/\sqrt{r}$ singularity of the stress at a crack tip. The average stress over the element at the fracture tip can then be estimated as

$$\sigma_a = \frac{\int_0^{h/2} \int_0^{\pi} \sigma_{rr} r \, d\phi \, dr}{\int_0^{h/2} \int_0^{\pi} r \, d\phi \, dr} = \frac{4\sqrt{2}C}{3\sqrt{h}} \tag{33}$$

when the stress in the radial direction is approximated as $\sigma_{rr} = C/\sqrt{r}$. Figure 7 shows an element at a crack tip. We have that strain is proportional to stress, which implies that the strain in the fracture tip element scales as

$$\epsilon \sim \frac{1}{\sqrt{h}} \sim \sqrt{N} \tag{34}$$

This is precisely the behaviour seen in Figure 6. The resolution dependence of the bond-strain implies that the fracture thresholds, which are assigned to the bonds,

must be scaled accordingly. Therefore, these thresholds have to be scaled with a factor $\sqrt{f}$ if the number of nodes is increased by a factor f. It is also possible to estimate the strain at the fracture tips in terms of stress using that $\sigma_a \approx E\Delta h/h$, which gives that

$$\frac{\Delta h}{h} \approx \frac{4\sqrt{2}}{3}\frac{C}{E\sqrt{h}} \tag{35}$$

is the strain corresponding to the parameter C. This parameter can be related to fracture toughness for homogeneous rocks since it is proportional to the stress intensity factor.

This criterion handles tensile (mode I) fracturing but not shear (mode II) fracturing. Shear fracture could also be dealt with by introducing a threshold for the deformation angle between two bonds that are initially right-angled, since the grid has initially square elements.

10. Hydraulic fracture of homogeneous rock

Numerical experiments are first carried out on a homogeneous rock, where all bonds have the same strength in terms of maximum allowed strain. Fluid pressure is created by injection of water at a constant rate $Q = 5 \cdot 10^{-4}$ m^3 s^{-1} at the centre of a 2D grid. It has the size 100m $\times$ 100m with 40×40 nodes. The pressure build-up from the chosen rate is first studied in case of no fracturing, and Figure 8 shows the results. The well pressure reaches nearly 2.5 MPa after 18.5 min of injection, and a little more than 4 MPa after 167 min. The pressure is then starting to rise at the boundaries too. Figure 8 also shows Theis solution (Theis, 1935; Wangen, 2010) given by

$$p(r,t) = \frac{\mu Q}{4\pi k_r\, dz}\,\mathrm{E}_1\left(\frac{\phi c_f \mu r^2}{4k_r t}\right) + p_0 \tag{36}$$

which gives the pressure at the time t and at a radial distance r from an injection well in an infinite 2D aquifer. Theis solution is a useful mean to estimate the pressure build-up at a given radius and time. The aquifer permeability is $k_r = 5 \cdot 10^{-14}$ m^2, the porosity $\phi = 0.2$, the fluid compressibility is $c_f = 1 \cdot 10^{-8}$ Pa^{-1} and the initial pressure is $p_0 = 0$ MPa. The pressure, equation (36), can also be written as

$$p(r,t) = p_c \mathrm{E}_1\left(\frac{t_r}{t}\right) \tag{37}$$

where

$$p_c = \frac{\mu Q}{4\pi k_r\, dz} \quad \text{and} \quad t_r = \frac{\phi c_f \mu r^2}{4 k_r t} \tag{38}$$

are a characteristic pressure and the characteristic time for the radius r, respectively. We see that the pressure at radius r and at time t_r is $p_r = p_c\, \mathrm{E}_1(1) \approx 0.2\, p_c$. The data for this case and a radius $r = 50$ m gives that $t_r = 417$ min and $p_r = 0.2$ MPa.

Figure 9a shows the well pressure in case of hydraulic fracturing during a time span of 50000 s (13.8 h). We notice that the initial pressure rise has an exponential form before the first fracture event, which happens after 15000 s (4.2 h). The pressure would have approached steady state if the rock had not fractured. The well pressure then drops with more than 1 MPa, before it starts to rise once more. The first event is followed by a train of fracture events, which has a well pressure between 2 MPa and 3.5 MPa. Figure 9b shows that one bond is broken in each of the events, which is as expected for a homogeneous rock where all bonds have the same strength. The pressure needs to rebuild before a new fracture event can happen, and Figure 10 shows in detail how the pressure rebuilds between the events.

The fluid flow in the rock surrounding the fracture is shown in Figure 11 when steady state is reached. The well pressure has then reached 2.5 MPa and it is insufficient for new bonds to become overstretched and break. Figure 11 shows how the fluid that is injected into the fracture leaks into the rock at steady state. The computed displacements are multiplied by a suitable factor in order to visualize the opening of the fracture. At steady state the injection rate is equal to the leakage through the fracture walls, and also equal to the leakage through the external boundaries.

It is the effective stress that is the cause for rock strain. Figure 12 shows the concentration of effective stress at the fracture tips at steady state, which is for the same state as for the fluid flow Figure 11. The stress concentration is symmetric around the fracture, which therefore develops symmetrically around the injection well.

The well pressure and the fracture events for the same case, but a lower rock permeability is shown in Figure 13. The permeability is $k_r = 1 \cdot 10^{-15}$ m^2 (a factor 50 less), and the time span for the same number of bonds to be broken is therefore reduced by the same factor. A lower permeability implies that the well

pressure increases more rapidly, and almost linearly, for the same injection rate. The fracture events are therefore more evenly distributed.

The intermittent behaviour of this model makes it different from the two classical models of hydraulic fracturing, the KDG-model (Khristianovic and Zheltov, 1955; Geertsma and de Klerk, 1969) and the PKN-model (Perkins and Kern, 1961; Nordgren, 1972). Both these models assume elliptical fractures, and the KGD-model is similar to the proposed numerical model by assuming plain-strain in the xy-plane. The fracture length is proportional to $t^{1/2}$ and $t^{1/4}$ for the KDG- and PKN-models, respectively, in case of permeable rock and high fluid loss (Piggott and Elsworth, 1996). The fracture length is proportional to $t^{2/3}$ and $t^{4/5}$, respectively, in the other regime of impermeable rock and no fluid loss (Piggott and Elsworth, 1996). The number of broken bonds is a measure for the length of a linear fracture and Figure 9b shows an example of how the fracture length grows as a function of time for a permeable rock. A difference between this model and the KDG- and PKN-models is that some time passes before the pressure has increased sufficiently to break the first bond and start the fracture propagation. Figure 11 shows the linear fracture at steady state, when the leak-off through the sides is equal to the injection rate. Another difference is that the fracture stops growing when the steady-state pressure is not sufficient to break another bond.

11. Hydraulic fracture of heterogeneous rock

A heterogeneous rock is modelled by assigning random strength to the bonds in the finite element grid. The grid is $100\text{m} \times 100\text{m}$ with 120×120 nodes. The bonds are made heterogeneous by setting $r = -0.3$ in the distribution given by (7). The bonds can then be divided into two groups with respect to strength – one where it is close to the average bond strength $\bar{s}$ and another where the strength is much weaker than $\bar{s}$. The rock permeability is $k_r = 1 \cdot 10^{-17}$ m^2 and the injection rate is $Q = 2.78 \cdot 10^{-4}$ m^3 s^{-1}. The time constant, equation (38), for Darcy flow towards the boundaries rock becomes $t_c = 4$ years. The low rock permeability compared to the two previous cases gives less fluid leakage through the fracture walls, and it makes the time scale of the fracture process much smaller.

Figure 14a shows the well pressure as function of time. We notice that the fracture events are non-evenly distributed and that several bonds are broken in each fracture event. A fracture event leads to a broken bond and the need for a recomputation of the fracture pressure. The reduced well pressure and the new state of stress

may by sufficient for new bonds along the fracture surface to be overstretched. The recomputation of well pressure and the breaking of the most overstretched bond continues until there are no more bonds to break. The fracture propagates by avalanches of broken fractures as can be seen from Figure 14b, which shows number of broken bonds in each event. This is in contrast to the case of an homogeneous rock having bonds of equal strength, where one bond at a time is broken. The well injection and fracturing are stopped at time 400 s, before the fracture gets close to the boundaries.

Figure 15 shows the fracture and the surrounding effective stress. The stress concentration at fracture tips are clearly seen and also the compression of the rock along the fracture sides. Negative stress is tension and positive stress is compression. The heterogeneous strength distribution of the bonds leads to the irregular fracture surface and the beginning of branching of the fracture.

12. Conclusion

A finite element procedure is presented for hydraulic fracturing. It is based on the Biot equations for coupled fluid flow and deformations in the rock, and a finite element formulation for the fluid pressure in the fracture. The fracture volume enters the pressure equation for the fracture by means of the fracture porosity. The formulation allows for a unified representation of both the fracture and rock on the same regular finite element grid.

Fracturing of the rock is based on the strength of the bonds (element sides) connecting the nodes. The reservoir is gridded with square elements with a typical size $1\text{m} \times 1\text{m}$. The elements change properties from rock to fracture as bonds are stretched beyond their strength threshold and break. A fractured element gets an increased permeability and a (almost) zero Young's modulus. The coarse representation of the fractures is sufficient to model the fluid flow in the fracture zone, the associated pressure gradients that open the fracture and the stress concentration at the fracture tips. The grid size captures the macroscopic propagation of fractures which are much larger than the element size.

It is assumed that a fracture event happens instantaneously and that the fluid volume in the fracture remains the same after an event of bond breaking. The pressure drop in the fracture that follows the breaking of a bond is computed with a procedure that preserves the fluid volume in the fracture.

The finite element formulation of the Biot equations for coupled Darcy flow and deformations are compared with exact solutions for the special case of 1D. These solutions show how the displacement from a fluid pressure applied in the fracture decreases with increasing leakage through the fracture walls, as the pressure gradient decreases.

It is shown that the bond-strain scales as $\sqrt{N}$ where N is the number of nodes in one lateral direction. This scaling is shown to follow from the $1/\sqrt{r}$ singularity at the fracture tips. The bond strength must therefore be scaled accordingly when the grid resolution is changed.

Two computational examples of hydraulic fracturing are shown, where both have fluid injected at a constant rate at the centre of the grid: one for a reservoir of homogeneous rock and another of heterogeneous rock. The pressure build-up from the injection well is validated against Theis' solution. The case of homogeneous rock gives a straight fracture that propagates symmetrically around the well. The fracturing of homogeneous rock is by a train of fracture events where one bond breaks in each event. A period of pressure build-up is necessary after a bond has broken before the pressure is sufficiently large for a new bond to become overstretched and break.

The example of a heterogeneous reservoir shows that hydraulic fracturing becomes an intermittent process in terms of broken bonds. There are random lengths of the periods of pressure build up between the fracture events. During the subsequent pressure drop several new bonds may be sufficiently weak and break.

13. Acknowledgement

The author is grateful for the suggestions and corrections to the manuscript made by editor Birol Dindoruk and an anonymous reviewer. This work has been partly funded by the Inject project supported by the Research Council of Norway.

14. Appendix: The finite element formulation

A multiplication of the force balance (1) with the basis function N_I associated with node I, and integration over the volume V gives that

$$\int_V \frac{\partial \sigma_{ij}}{\partial x_j} N_I dV = \int_V \left(\frac{\partial \sigma'_{ij}}{\partial x_j} + \alpha \frac{\partial p}{\partial x_i} \right) N_I dV = 0 \tag{39}$$

in terms of effective stress σ'_{ij}. Upper case indices, like I and J, denote node numbers and lower case indices i and j are spatial directions. (Einstein summation convention is applied, which assumes summation of pairs of equal indices.) A use of the divergence theorem and partial integration of equation (39) give the Galerkin formulation

$$\int_V \sigma'_{ij} \frac{\partial N_I}{\partial x_j} dV = \int_V \alpha \frac{\partial p}{\partial x_i} N_I dV \tag{40}$$

The integral of effective stress over the boundary is left out because of Dirichlet boundary conditions. We impose zero displacement for the boundary nodes onto the equation system. The Galerkin formulation with the displacements as the unknowns becomes simplified by using the following standard notation (Huyakorn and Pinder, 1983; Langtangen, 1999). Stress and strain written as the vectors

$$\boldsymbol{\sigma}' = (\sigma'_{xx},\ \sigma'_{yy},\ \sigma'_{xy}) \quad \text{and} \quad \boldsymbol{\epsilon} = (\epsilon_{xx},\ \epsilon_{yy},\ 2\epsilon_{xy}) \tag{41}$$

allow for the compact notation

$$\begin{bmatrix} \sigma'_{1j} \frac{\partial N_I}{\partial x_j} \\ \sigma'_{2j} \frac{\partial N_I}{\partial x_j} \end{bmatrix} = \mathbf{B}_I^T \boldsymbol{\sigma}' \tag{42}$$

and

$$\boldsymbol{\epsilon} = \mathbf{B}_J \mathbf{u}_J \tag{43}$$

where derivatives of the basis function appears in the matrix

$$\mathbf{B}_I = \begin{bmatrix} \frac{\partial N_I}{\partial x} & 0 \\ 0 & \frac{\partial N_I}{\partial y} \\ \frac{\partial N_I}{\partial y} & \frac{\partial N_I}{\partial x} \end{bmatrix} \tag{44}$$

The vector $\mathbf{u}_J = (u_{Jx}, u_{Jy})$ is the displacement in the x- and y-direction at node J. The Lamé-equations (2) becomes $\boldsymbol{\sigma} = \mathbf{D}\boldsymbol{\epsilon}$ when expressed with the stress- and strain vectors, where $\mathbf{D}$ is the matrix

$$\mathbf{D} = \begin{bmatrix} (2G+\lambda) & 0 & 0 \\ 0 & (2G+\lambda) & 0 \\ 0 & 0 & G \end{bmatrix} \tag{45}$$

The Galerkin formulation (40) can now be re-expressed in terms of the displacements as

$$\int_V \mathbf{B}_I^T \mathbf{D}\, \mathbf{B}_J \mathbf{u}_J = \int_V \alpha \nabla p\, N_I\, dV \tag{46}$$

The pressure gradient on the right-hand-side is the load that causes the displacements.

The pressure p_J^n is a solution of the following standard Galerkin formulation (Huyakorn and Pinder, 1983; Langtangen, 1999)

$$\left(\int_V C N_I N_J\, dV + \Delta t \int_V \frac{k}{\mu} \nabla N_I \nabla N_J\, dV \right) p_J^n \tag{47}$$

$$= \int_V C N_I N_J\, dV p_J^{n-1} + \Delta t \int_V Q\, N_I\, dV \tag{48}$$

which is obtained from the pressure equations (6) and (11) by multiplication by the basis function N_I and the use of Greens theorem. The surface integral from Greens theorem drops out because of Dirichlet boundary conditions. Time discretization is backward Euler, where p^n and p^{n-1} are the pressures at the present and previous time step, respectively. The coefficient C is

$$C = \begin{cases} \phi c_f & \text{(rock elements)} \\ \phi_c c_f & \text{(fracture elements)} \end{cases} \tag{49}$$

and the source term is

$$Q = \begin{cases} -\alpha\, \partial\epsilon/\partial t & \text{(rock elements)} \\ -\partial\phi_c/\partial t & \text{(fracture elements, but not well)} \\ Q_{\text{in}}/h^2 & \text{(well element)} \end{cases} \tag{50}$$

The equations for pressure and strain are solved decoupled at each time step. The pressure equation is solved first. The pressure at the current time step is then used in the right-hand-side of the equation for the displacements, which gives the displacements at the current time-step. The time-derivative of the fracture porosity and the volume strain in the rock are from the previous time step.

References

Adachi, J., Siebrits, E., Peirce, A., Desroches, J., 2007. Computer simulation of hydraulic fractures. International Journal of Rock Mechanics and Mining Sciences 44, 739–757.

Al-Busaidi, A., Hazzard, J., Young, R., 2005. Distinct element modeling of hydraulically fractured Lac du Bonnet granite. Journal of Geophysical Research 110, 1–14.

Alava, M., Nukala, P., Zapperi, S., 2006. Statistical models of fracture. Advances in Physics 55, 349–476.

Bernabé, Y., 1995. The transport properties of networks of crakcs and pores. Journal of Geophysical Research 100, 4231–4241.

Biot, M., 1941. General theory of three dimensional consolidation. Journal of Applied Physics 12, 155–164.

Brown, S., Caprihan, A., hardy, R., 1998. Experimental observation of fluid flow in a single fracture. Journal of Geophysical Research 103, 5125–5132.

Cheng, Y., Lee, W., McVay, D., 2007. A new approach for reliable estimation of hydraulic fracture properties in tight gas wells. SPE 105767, 1–12.

Davis, G., Reynolds, S., 1996. Structural geology of rock and regions. John Wily & Sons.

Evans, K., Moriya, H., Niitsuma, H., Jones, R., Phillips, W., Genter, A., Sausse, J., Jung, R., Baria, R., 2005. Microseismicity and permeability enhancement of hydrogeologic structures during massive fluid injections into granite at 3 km depth at the Soultz HDR site. Geophysical Journal International 160, 388–412.

Flekkøy, E., Malthe-Sørenssen, A., Jamtveit, B., 2002. Modeling hydrofracture. Journal of Geophysical Research 107, ECV1–1–11.

Geertsma, J., de Klerk, F., 1969. A rapid method of predicting width and extent of hydraulically induced fractures. Journal of Petroleum Technology 21, 1571–1581.

Helland, K., 1984. Introduction to Fracture Mechanics. McGraw-Hill Inc.

Herrmann, J., Roux, S., 1990. Statistical models for the fracture of disordered media. North-Holland, Amsterdam.

Hubbert, M., Willis, D., 1957. Mechanics of hydraulic fracturing. Petroleum Transactions AIME 210, 153–168.

Huyakorn, P., Pinder, G., 1983. Computational methods in subsurface flow. Academic Press, Inc.

Jackson, M., Cheadle, M., Atherton, M., 2003. Quantitative modeling of granitic melt generation and segregation in the continental crust. Journal of Geophysical Research 108, 1–21.

Jaeger, J., Cook, N., Zimmerman, R., 2007. Fundamentals of rock mechanics, fourth edition. Blackwell Scientific Publications.

Judd, A., Hovland, M., 2007. Seabed fluid flow. Impact on Geology, Biology and the Marine Environment. Cambridge University Press.

Khristianovic, S.A., Zheltov, Y.P., 1955. Formation of vertical fractures by means of highly viscous liquid, in: Proceedings of the 4th World Petroleum Congress, Rome, pp. 579–586.

Kvamme, B., Liu, S., 2009. Reactive transport of CO2 in saline aquifers with implicit geomechanical analysis. Energy Procedia 1, 3267–3274.

Langtangen, H., 1999. Computational partial differential equations: Numerical methods and Diffpack programming. Springer.

Måløy, K., Santucci, S., Schmittbuhl, J., Toussaint, R., 2006. Local waiting time fluctuations along a randomly pinned crack front. Physical Review Letters 96, 045501.

Måløy, K., Schmittbuhl, J., Hansen, A., Batrouni, G., 2003. Scaling and dynamics of an interfacial crack front. International Journal of Fracture 121, 9.

Nordgren, R., 1972. Propagation of a vertical hydraulic fracture. SPE Journal 12, 306–314.

Perkins, T., Kern, L., 1961. Widths of hydraulic fractures. Journal of Petroleum Technology 13, 937–949.

Piggott, A., Elsworth, D., 1996. Displacement of formation fluids by hydraulic fracturing. Géotechnique 46, 671–681.

Rector, J., Qicheng, D., Patzek, T., 2000. Passive characterization of hydrofracture properties using signals from hydraulic pumps. Journal of Petroleum Science and Engineering 27, 49–58.

Rutqvist, J., Tsang, C.F., 2002. A study of caprock hydromechanical changes associated with CO2-injection into a brine formation. Environmental Geology 42, 296–305.

Sanjuan, B., Pinault, J.L., Rose, P., Gérard, A., Brach, M., Braibant, G., Crouzet, C., Foucher, J.C., Gautier, A., Touzelet, S., 2006. Tracer testing of the geothermal heat exchanger at Soultz-sous-Forêts (France) between 2000 and 2005. Geothermics 35, 622–653.

Sasaki, S., 1998. Characteristics of microseismic events induced during hydraulic fracturing experiments at the Hijiori hot dry rock geothermal energy site, Yamagata, Japan. Tectonophysics 289, 171–188.

Settari, A., 1979. Simulation of the hydraulic fracturing process. SPE 7693, 187–202.

Sibson, R., 1992. Implications for fault-valve behaviour for rupture nucleation and recurrence. Tectonophysics 211, 283–293.

Sneddon, I., Elliott, H., 1946. The opening of a Griffith crack under internal pressure. Q. Appl. Math. 4, 262–267.

Tang, C., Tham, L., Lee, P., Yang, T., Li, L., 1992. Coupled analysis of flow, stress and damage (FSD) in rock failure. International Journal of Rock Mechanics and Mining Sciences 39, 477–489.

Theis, C., 1935. The relation between the lowering of the piezometric surface and the rate and duration of discharge of a well using groundwater storage. Trans. Am. Geophys. Union 2, 519–524.

Turcotte, D., Morgan, J., 1992. The physics of magma migration and mantle flow beneath a mod-ocean ridge. Geophysical monograph, AGU 71, 151–182.

Tzschichholz, F., Herrmann, H., 1995. Simulations of pressure fluctuations and acoustic emission in hydraulic fracturing. Phys. Rev. E 51, 1961–1970.

Tzschichholz, F., Herrmann, H., Roman, H., M., P., 1994. Beam model for hydraulic fracturing. Phys. Rev. B 49, 7056–7059.

Tzschichholz, F., Wangen, M., 1998. Modelling of hydraulic fracturing of porous materials, in: Aliabadi, M. (Ed.), Fracture of Rock. WIT Press, Southhampton. chapter 8, pp. 227–260.

Wang, H., 2000. Theory of linear poroelasticity. Princeton University Press.

Wang, S., Sun, L., Au, A., Yang, T., Tang, C., 2009. 2D-numerical analysis of hydraulic fracturing in heterogeneous geo-materials. Construction and Building Materials 23, 2196–2206.

Wangen, M., 2001. A quantitative comparison of some mechanisms generating overpressure in sedimentary basins. Tectonophysics 334, 211–234.

Wangen, M., 2010. Physical principles of sedimentary basin analysis. Cambridge University Press.

Weng, X., Settari, A., Keck, R., 1997. A field demonstration of hydraulic fracturing for solid waste disposal - injection pressure analysis. International Journal of Rock Mechanics and Mining Sciences 34, paper no. 331.

15. Captions

Figure 1. *The fracture has a volume V, and the elements crossed by the fracture have a total volume V_E. The illustration exaggerates the fracture aperture. The dashed lines show broken bonds.*

Figure 2. *The 1D solution (23) for fluid pressure is plotted as a function of time. The fluid pressure is initially zero, and it becomes $p_0 = 10$ MPa at time $t = 0$. During time it approaches the linear steady state pressure.*

Figure 3. *The 1D x-displacement from equation (18) is plotted for the fluid pressure in Figure 2. The absolute value of the displacements at $x = l$ become reduced to the half as the fluid pressure approaches the stationary state.*

Figure 4. *The absolute value of the displacement at the fracture wall (at $x = l$) is plotted as a function of time. The displacement is given by the pressure in Figure 2.*

Figure 5. *The elastic energy per unit cross section stored in the rock of length $x = l$ as a function of time for the fluid pressure in Figure 2.*

Figure 6. *The strain of the bonds of at the tips of straight fracture as a function of the grid resolution. The resolution is measured in terms of number of nodes N in one spatial direction.*

Figure 7. *(a) A straight fracture is represented by the open (white) elements. A possible outline of a fracture is also shown. (b) The averaging of the stress is over a half-circle in the element at the fracture tip.*

Figure 8. *The pressure build-up in the well in case fracturing does not take place.*

Figure 9. *(a) The well pressure in the hydraulic fracturing of a homogeneous rock. The fluid pressure in case of no fracturing is shown in Figure 8. The drops in fluid pressure are caused by fracture events. (b) Only one bond is broken in each fracture event.*

Figure 10. *The pressure increase between fracture events.*

Figure 11. *The straight fracture when the fluid pressure has reached steady state. It is seen that the fluid flow acts to open the fracture.*

Figure 12. *The effective stress for the fracture under stationary fluid flow, which is shown in Figure 11. (a)* σ'_{xx}*. (b)* σ'_{yy}*. The figures (a) and (b) show the fractured elements and the broken bonds.*

Figure 13. *(a) The well pressure in the hydraulic fracturing of a homogeneous rock but less permeable rock than in Figure 9. The black bullets mark the time steps. The drops in fluid pressure are caused by fracture events. (b) The number of bonds that are broken in each fracture event.*

Figure 14. *(a) The well pressure in case of hydraulic fracturing of a heterogeneous and low permeable rock. The black bullets mark the time steps. (b) The jumps in the number of broken bonds show the fracture events.*

Figure 15. *The effective stress for the fracture at the end of the simulation shown in Figure 14. (a)* σ'_{xx}*. (b)* σ'_{yy}*. The figures (a) and (b) show the fractured elements and the broken bonds.*

16. Figures

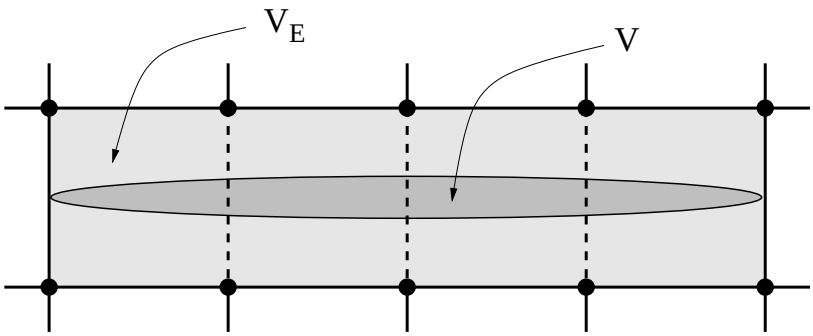

Figure: 1

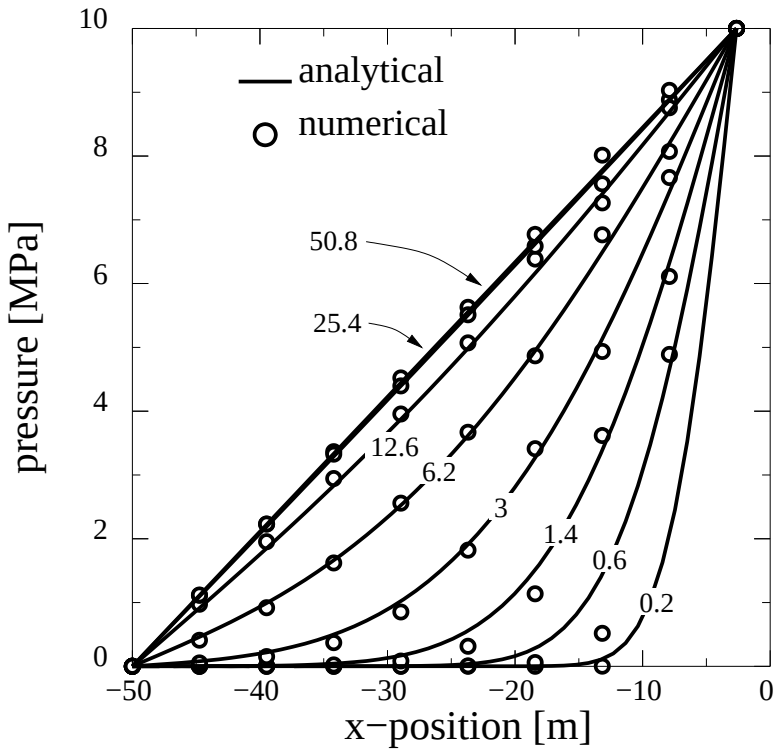
analytical
numerical
50.8
25.4
12.6
6.2
3
1.4
0.6
0.2
pressure [MPa]
x−position [m]
10
8
6
4
2
0
−50
−40
−30
−20
−10
0

Figure: 2

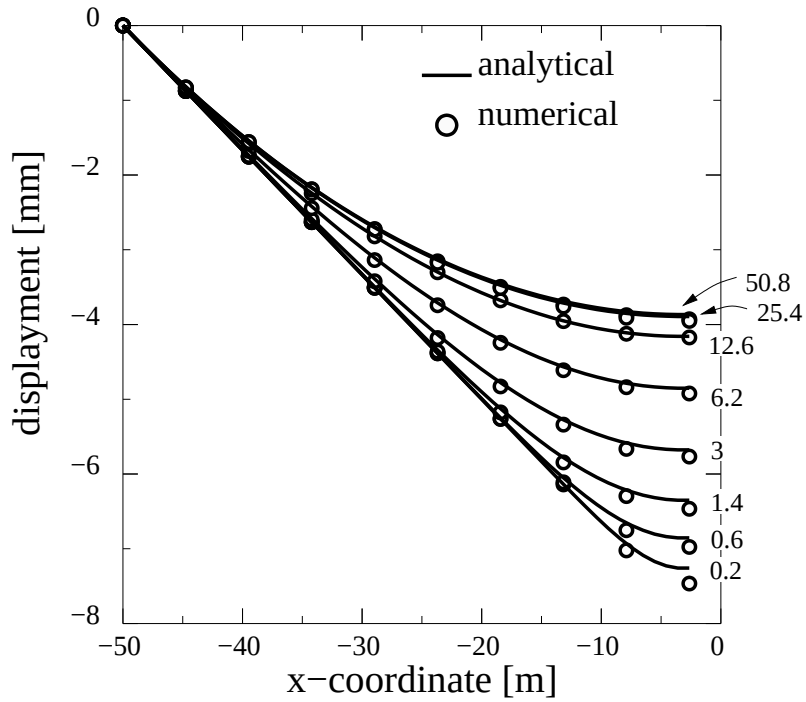
analytical
numerical
displayment [mm]
x−coordinate [m]
0
−2
−4
−6
−8
−50
−40
−30
−20
−10
0
50.8
25.4
12.6
6.2
3
1.4
0.6
0.2

Figure: 3

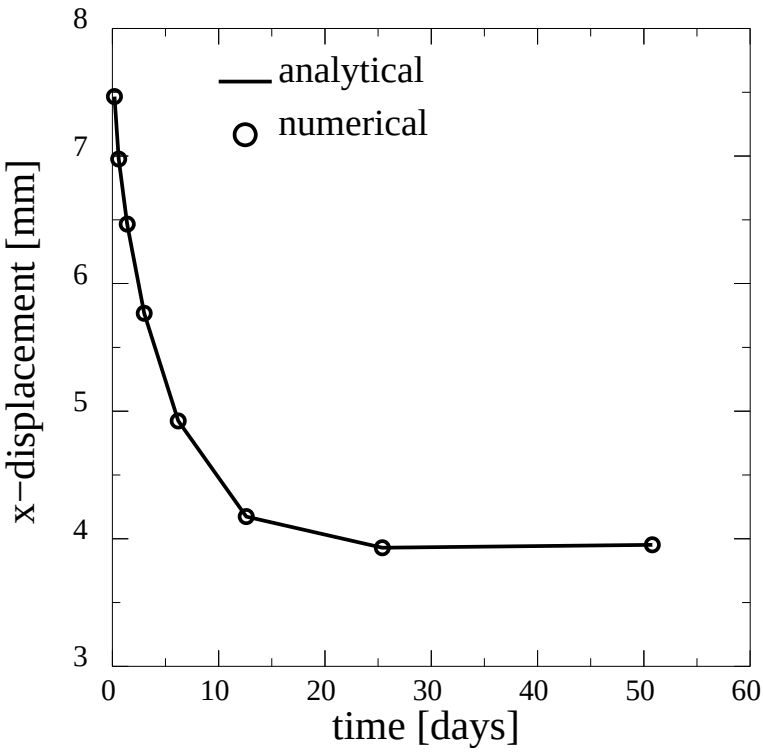
analytical
numerical
x−displacement [mm]
time [days]
8
7
6
5
4
3
0
10
20
30
40
50
60

Figure: 4

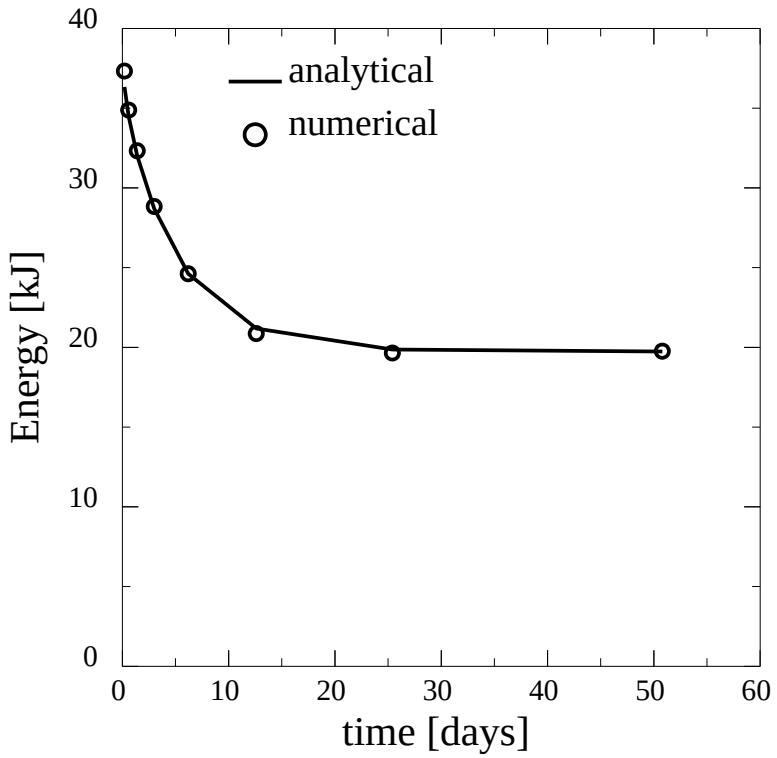
40
30
20
10
0
0
10
20
30
40
50
60
Energy [kJ]
time [days]
analytical
numerical

Figure: 5

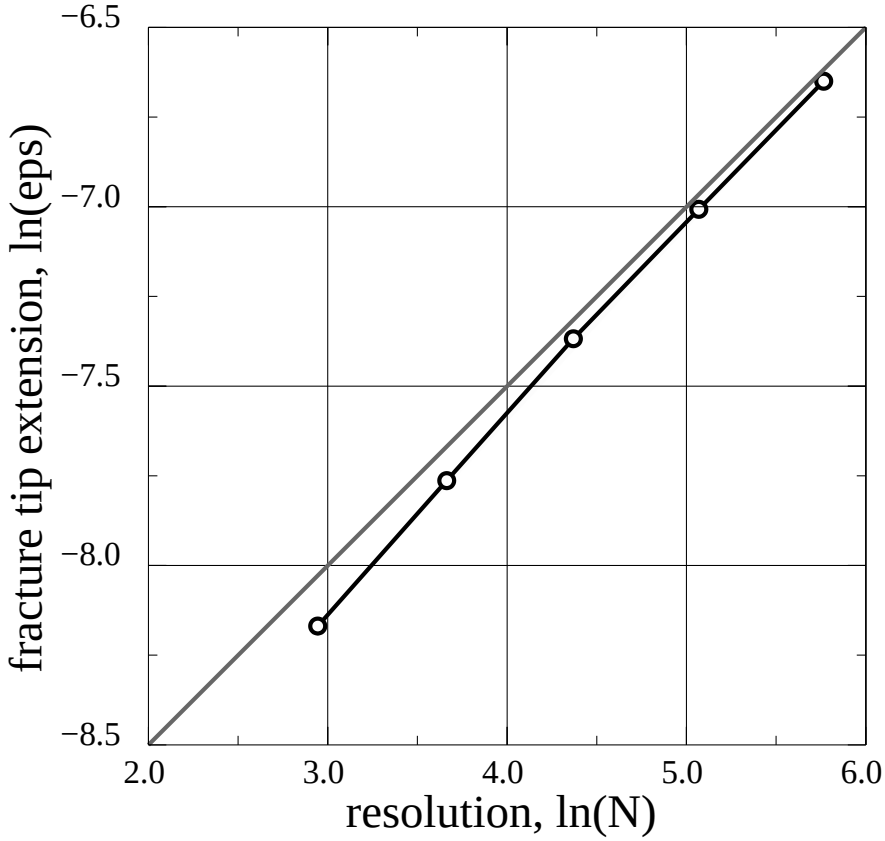
−6.5
−7.0
−7.5
−8.0
−8.5
2.0
3.0
4.0
5.0
6.0
fracture tip extension, ln(eps)
resolution, ln(N)

Figure: 6

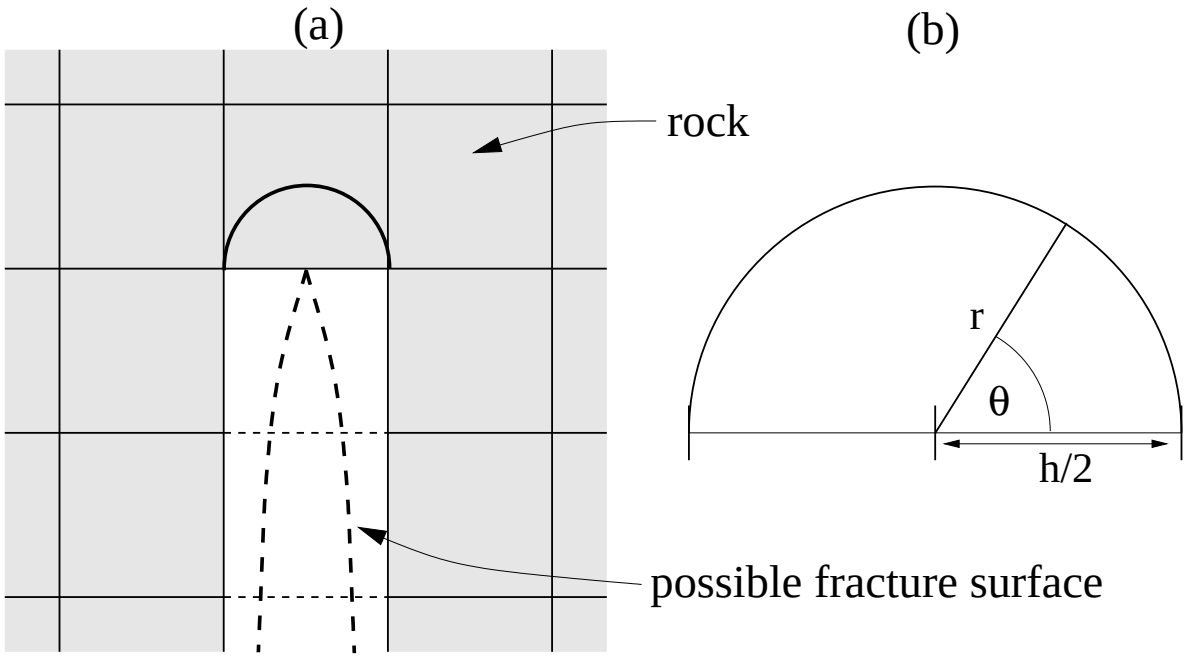

Figure: 7

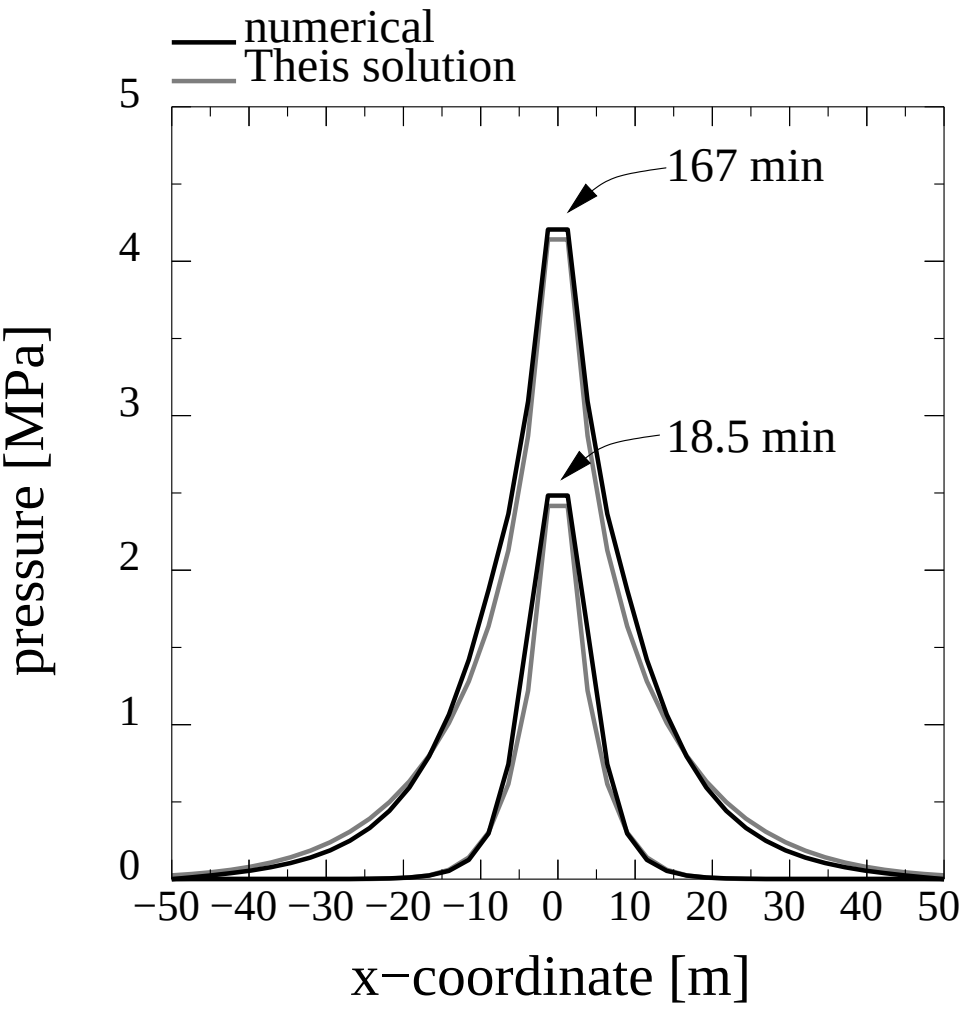
numerical
Theis solution
167 min
18.5 min
pressure [MPa]
x−coordinate [m]
0
1
2
3
4
5
−50
−40
−30
−20
−10
0
10
20
30
40
50

Figure: 8

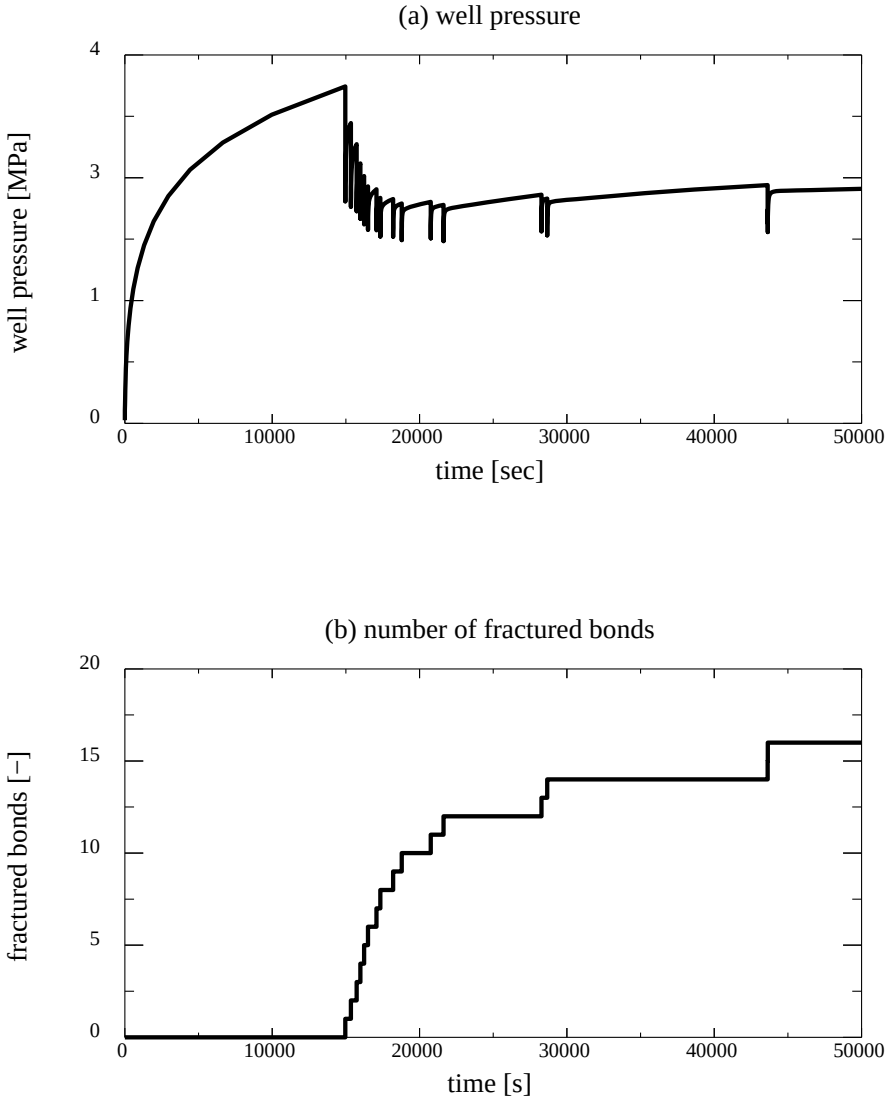
(a) well pressure
well pressure [MPa]
4
3
1
0
0
10000
20000
30000
40000
50000
time [sec]
(b) number of fractured bonds
fractured bonds [−]
20
15
10
5
0
0
10000
20000
30000
40000
50000
time [s]

Figure: 9

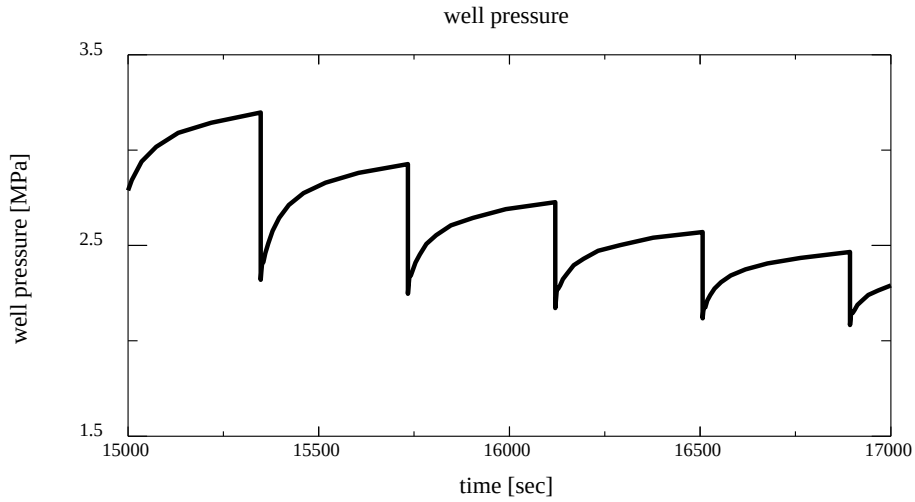
well pressure
3.5
2.5
1.5
well pressure [MPa]
15000
15500
16000
16500
17000
time [sec]

Figure: 10

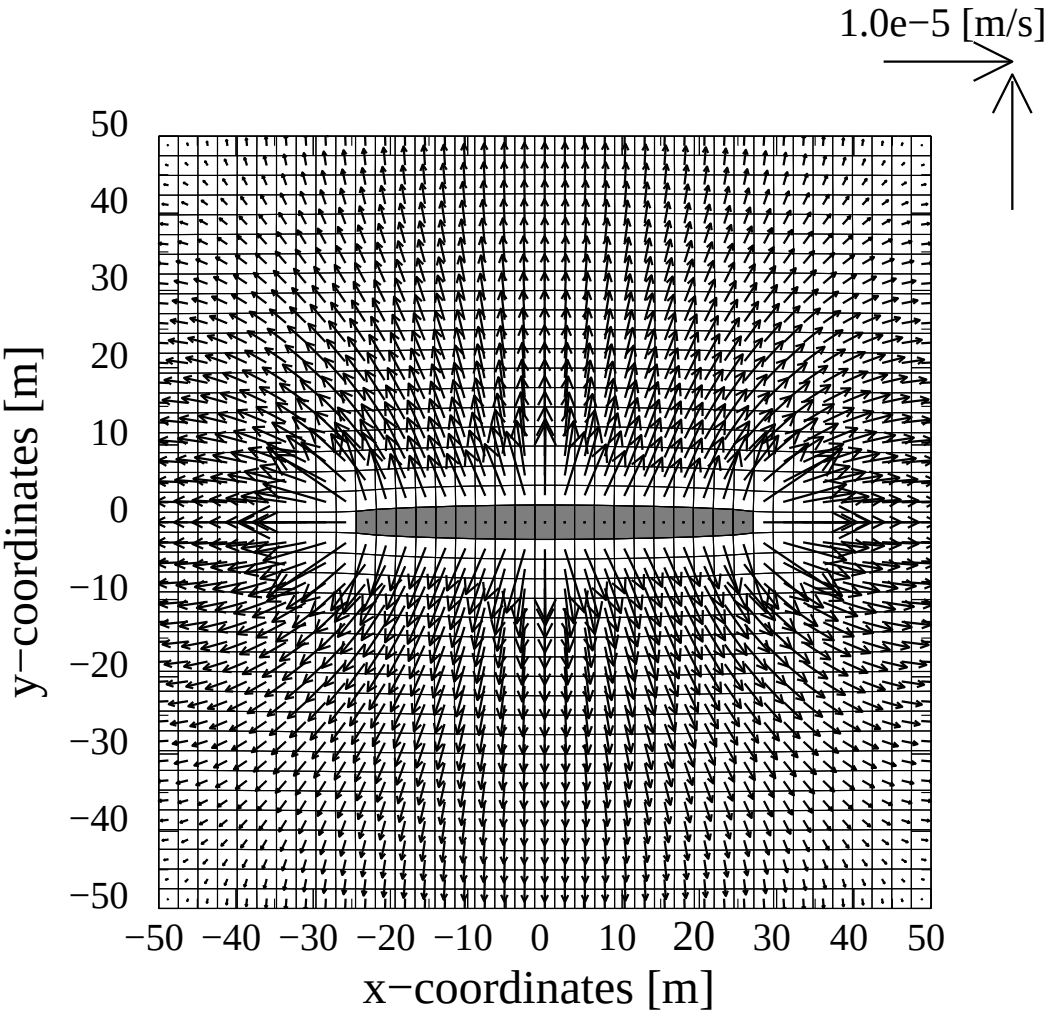
1.0e−5 [m/s]
50
40
30
20
10
0
−10
−20
−30
−40
−50
y−coordinates [m]
−50 −40 −30 −20 −10 0 10 20 30 40 50
x−coordinates [m]

Figure: 11

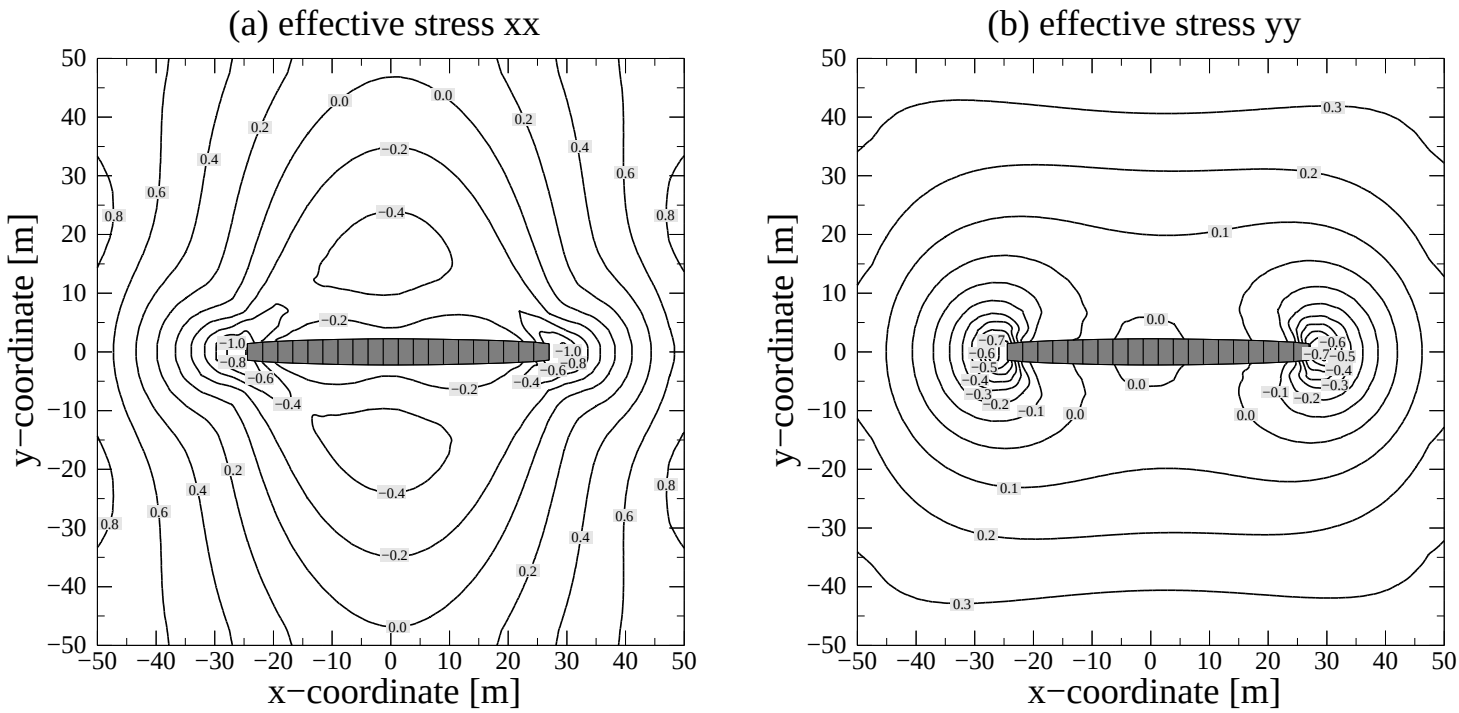
(a) effective stress xx
(b) effective stress yy
x−coordinate [m]
y−coordinate [m]

Figure: 12

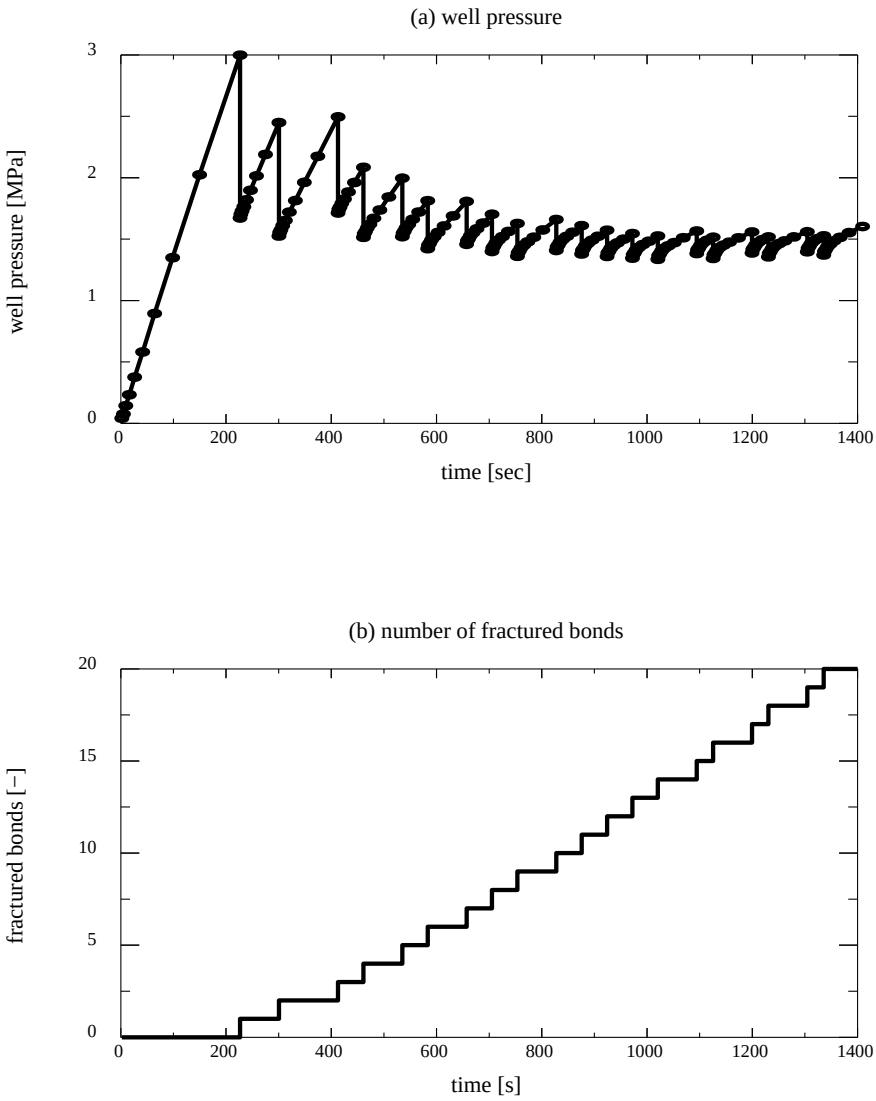
(a) well pressure
well pressure [MPa]
time [sec]
0
1
2
3
0
200
400
600
800
1000
1200
1400
(b) number of fractured bonds
fractured bonds [−]
time [s]
0
5
10
15
20
0
200
400
600
800
1000
1200
1400

Figure: 13

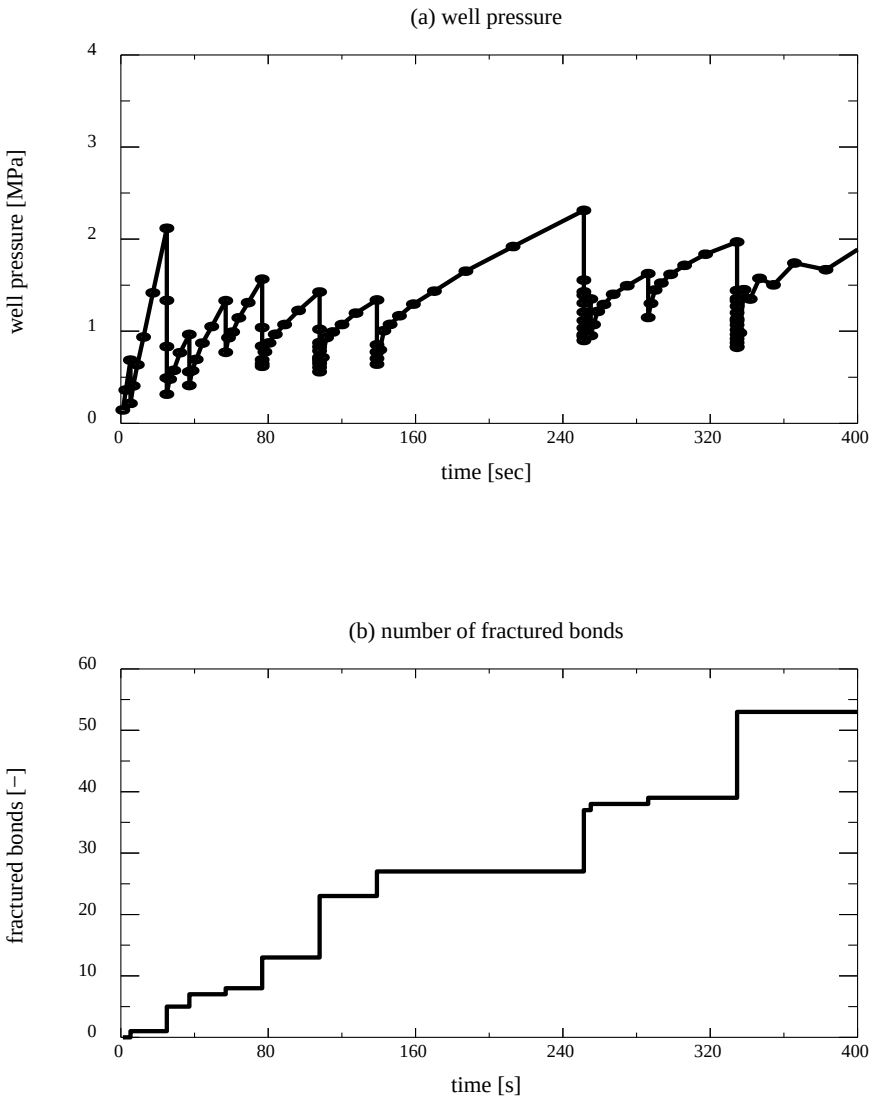
(a) well pressure
well pressure [MPa]
time [sec]
0
1
2
3
4
0
80
160
240
320
400
(b) number of fractured bonds
fractured bonds [−]
time [s]
0
10
20
30
40
50
60
0
80
160
240
320
400

Figure: 14

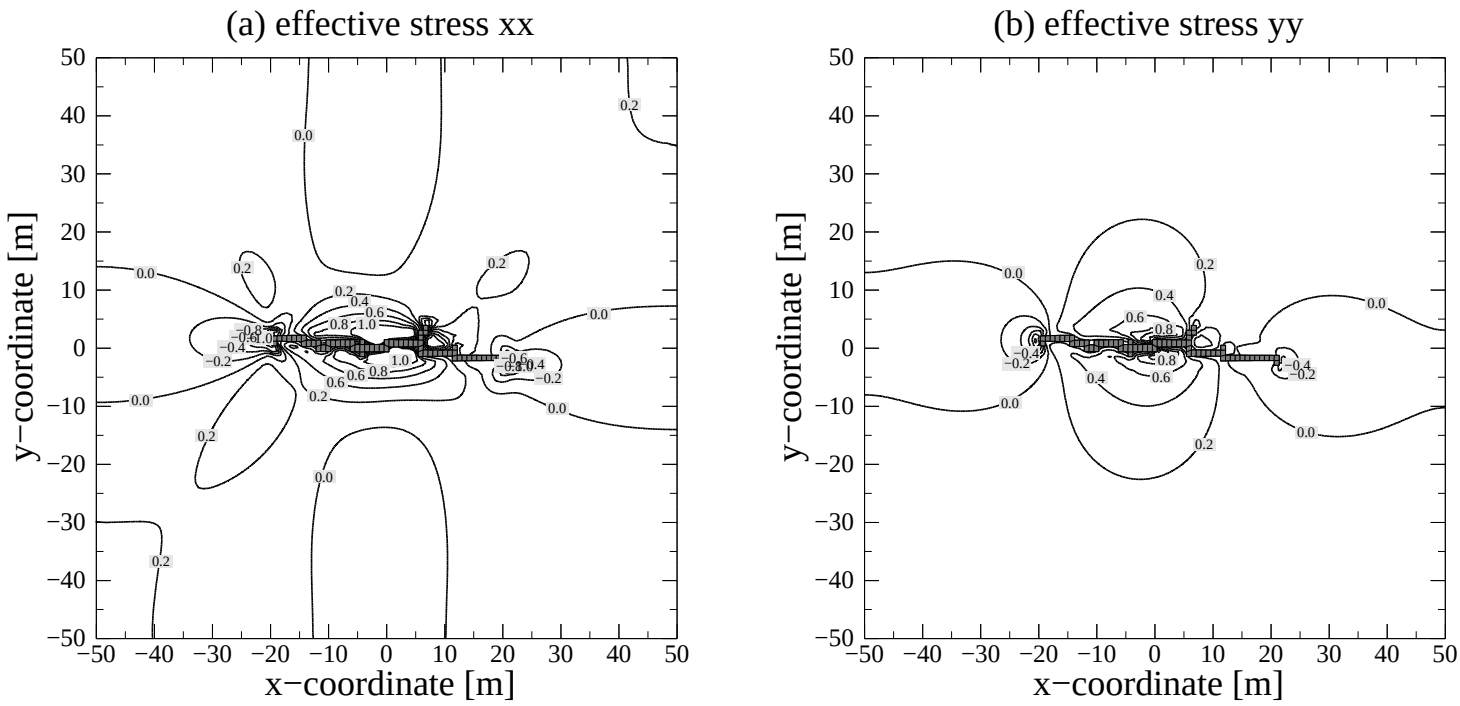
(a) effective stress xx
(b) effective stress yy
y−coordinate [m]
x−coordinate [m]

Figure: 15